Multidecadal Variability of the Overturning Circulation in Presence of Eddy Turbulence

THIERRY HUCK AND OLIVIER ARZEL

Laboratoire de Physique des Océans, UMR 6523 CNRS/IFREMER/IRD/UBO, Brest, France

FLORIAN SÉVELLEC

Ocean and Earth Science, National Oceanography Centre Southampton, University of Southampton, Southampton, United Kingdom

(Manuscript received 17 June 2014, in final form 8 October 2014)

ABSTRACT

At low-resolution, idealized ocean circulation models forced by prescribed differential surface heat fluxes show spontaneous multidecadal variability depending critically on eddy diffusivity coefficients. The existence of this critical threshold in the range of observational estimates legitimates some doubt on the relevance of such intrinsic oscillations in the real ocean. Through a series of numerical simulations with increasing resolution up to eddy-resolving ones (10 km) and various diapycnal diffusivities, this multidecadal variability proves a generic ubiquitous feature, at least in model versions with a flat bottom. The mean circulation largely changes in the process of refining the horizontal grid (along with the associated implicit viscosity and diffusivity), and the spatial structure of the variability is largely modified, but there is no clear influence of the resolution on the main oscillation period. The interdecadal variability appears even more robust to low vertical diffusivity and overturning when mesoscale eddies are resolved. The mechanism previously proposed for these oscillations, involving westward-propagating baroclinically unstable Rossby waves in the subpolar region and its feedback on the mean circulation, appears unaffected by mesoscale turbulence and is simply displaced following the polar front.

1. Introduction

The North Atlantic basin shows prominent variability on decadal (Deser and Blackmon 1993) to multidecadal (Kushnir 1994) time scales, the latter being referred to as the Atlantic multidecadal oscillation (AMO) or variability (AMV) (Delworth and Mann 2000). The AMO has often been related to variations of the meridional overturning circulation (Knight et al. 2005). Multiproxy and instrumental records reveal a low-frequency signal with a dominant period around 50–80 yr (Delworth et al. 2007), but recent analyses suggest also the existence of a much shorter time scale in the 20–30-yr range (Frankcombe and Dijkstra 2009; Chylek et al. 2011).

Various mechanisms have been proposed for similar variability appearing in coupled models (Delworth et al. 1993; Timmermann et al. 1998; Ba et al. 2013; among many others), but it is not yet clear if the atmosphere plays an active role (Weaver and Valcke 1998; Delworth and Greatbatch 2000). Another strong paradigm for the multidecadal variations in North Atlantic sea surface temperatures (SSTs) is a response to the atmospheric forcing, namely, through the North Atlantic Oscillation (NAO) (Eden and Jung 2001; Mecking et al. 2014). But whether the low-frequency NAO variability is a purely atmospheric process (James and James 1989) or is influenced by the underlying ocean remains the central and still open question. However, if a dominant multidecadal time scale emerges, it is possible that it is related to the ocean dynamics (advection, Rossby waves), for instance through an ocean mode, either unstable or damped. In the latter case, it can be sustained by the atmospheric coupling (Cessi and Paparella 2001) or by the atmospheric noise associated with midlatitude synoptic variability (Griffies and Tziperman 1995; Frankcombe et al. 2009; Sévellec et al. 2009).

At low (i.e., not eddy permitting) resolution, intrinsic interdecadal variability arises spontaneously in idealized

Corresponding author address: Thierry Huck, Laboratoire de Physique des Océans, Université de Bretagne Occidentale, UFR Sciences F308, 6 Avenue Le Gorgeu, CS 93837, 29238 Brest CEDEX 3, France.
E-mail: thuck@univ-brest.fr

DOI: 10.1175/JPO-D-14-0114.1

ocean circulation models forced by prescribed buoyancy fluxes when the overturning is large enough and the various dissipations low enough (Huang and Chou 1994; Greatbatch and Zhang 1995; Huck et al. 1999a). This often overlooked behavior has been interpreted as a large-scale baroclinic instability (Colin de Verdière and Huck 1999) sustaining Rossby waves propagating along the polar boundary and pacing the variations of the meridional and zonal overturning circulation (te Raa and Dijkstra 2002). The weak growth time scale, of the order of decades (certainly resulting from the large eddy viscosity and diffusivity acting on the large horizontal scales), makes the resulting oscillations extremely sensitive to additional damping, either as surface temperature restoring or eddy diffusivity (Huck et al. 2001). The existence of a critical threshold for the horizontal eddy diffusivity, close to 2000 $m^2 s^{-1}$ in Huck and Vallis (2001), that is, in the range of observational estimates (Ollitrault and Colin de Verdière 2002), casts some doubts on the relevance of such oscillations in the climate system, as does the damping effect from including variable bottom topography noted by Winton (1997). Preliminary experiments with increasing horizontal resolution down to eddy-permitting scales suggested the multidecadal oscillations were robust to the interaction with mesoscale turbulence (Huck et al. 2001), but computer time and storage 15 yr ago restricted drastically the number of experiments and the quantity of model output; a single simulation had been carried out at 20-km resolution.

Regarding the paradigm for the growth of such a large-scale baroclinic instability, the existence of a barotropic mode is not necessary in this instability, so the classical two-layer Phillips (1951) model is not adequate to capture the higher vertical wavenumber structure. The continuously stratified Eady–Charney model (Eady 1949; Charney 1947) is certainly relevant and that has been illustrated in Huck et al. (2001, their section 2c and Fig. 5). The use of large Laplacian eddy dissipation with nonzero beta effect shifts the maximum growth rate to larger scales, in agreement with the modes found in the nonlinear model. Given the surface-intensified stratification and shear, the instability probably arises from the interaction of low baroclinic modes (because of the associated decadal time scale) and no longer bottom and top edge waves as in the classical Eady model. Sévellec and Huck (2014, manuscript submitted to *J. Phys. Oceanogr.*) analyze a simple three-level model for the instability, suggesting a coupling between the first two baroclinic vertical modes.

In the meantime, theoretical work has suggested that Rossby waves fronts may be prone to baroclinic instability and break up into eddies along their westward propagation, eventually never reaching the western boundary (LaCasce and Pedlosky 2004; Isachsen et al. 2007). In addition, a large number of studies have addressed the low-frequency variability of the wind-driven circulation, for which the resolution of mesoscale eddies plays a major role in various types of idealized ocean (Dijkstra and Ghil 2005, and references therein) and coupled models (Kravtsov et al. 2006; Berloff et al. 2007a).

These different ideas led us to reconsider the sensitivity of the intrinsic variability of the thermally driven circulation to the horizontal resolution and mesoscale turbulence, first in idealized configurations for simplicity. In fact, a series of identical numerical experiments at various resolutions are rarely performed, although they provide some valuable insight into the models' uncertainty. For instance, Levy et al. (2010) led a series of experiments in an idealized North Atlantic double gyre configuration for resolutions ranging from 106 km down to 2 km, highlighting the influence of the submesoscale; however, their 100-yr-long integrations did not address the low-frequency variability. Such series of experiments are obviously far more complex to do in realistic configurations (Marsh et al. 2009) or even coupled models (Roberts et al. 2004; Bryan et al. 2006; Hodson and Sutton 2012), where some tuning is necessary (mixing and convection), but they prove that the meridional overturning stability and variability are often very sensitive to the resolution.

We report here on a series of experiments from 85- down to 10-km horizontal resolution, with a parallel increase in vertical resolution. As the processes responsible for horizontal eddy diffusivity are partly resolved, the next critical (and mostly unknown) parameter influencing the mean overturning circulation becomes the vertical/diapycnal mixing, and we explore a range of values from the low (10^{-5} $m^2 s^{-1}$) to the high (10^{-4}) ends (Waterhouse et al. 2014). We should make it clear that the objective of the paper is really to show the robustness of the large-scale multidecadal variability with respect to the oceanic mesoscale turbulence, through a brief description of a large set of (computationally demanding) numerical experiments. The results appear in good agreement with the oscillation mechanism proposed at non-eddy-resolving resolution, which will not be discussed further.

The paper is organized as follows: Section 2 describes the model, the configurations with increasing resolution, and the forcing. Section 3 describes the mean overturning circulation and temperature field, as a function of vertical mixing and horizontal resolution. Section 4 focuses on the mesoscale turbulence and its relationship with the mean circulation. The multidecadal variability is addressed in the central section 5, with emphasis on its patterns in temperature and overturning, whereas the oscillation period is discussed in section 6. Section 7

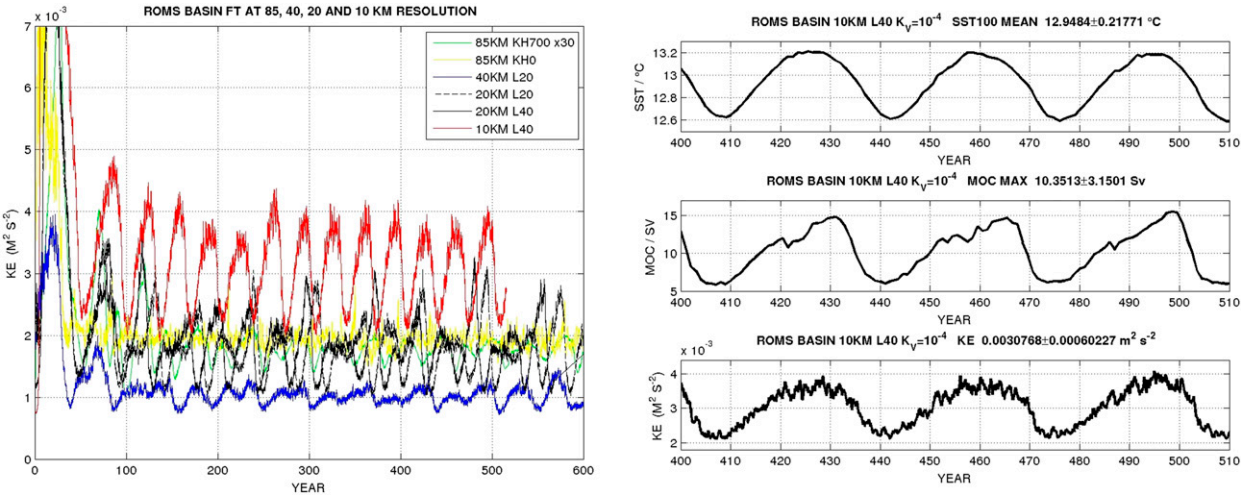

FIG. 1. (left) Total kinetic energy as a function of time in the reference case ($K_V = 10^{-4}\,\mathrm{m^2\,s^{-1}}$) for the whole range of horizontal and vertical resolutions. KE is computed online at daily frequency from instantaneous velocity fields. Note KE is multiplied by 30 for the lower-resolution case with explicit eddy diffusivity and viscosity ($K_H = 700$ and $A_H = 5\,10^4\,\mathrm{m^2\,s^{-1}}$, respectively). (right) Basin-averaged sea surface temperature (0–100 m), maximum of the MOC streamfunction (both based on annual-mean fields), and KE as described earlier for the 10-km reference case. The three evolve almost in phase.

provides a discussion regarding the Rossby waves' propagation against baroclinic instability at the eddy scale. Section 8 concludes and provides some perspectives.

2. Model configurations and forcing

Numerical experiments are performed with the Regional Ocean Modeling System (Shchepetkin and McWilliams 2005), based on topography-following sigma coordinates (although the basin will have a flat bottom), for simulating an idealized thermally driven ocean overturning circulation at various resolution. The model configuration spans from 20° to 60°N in latitude (4468 km) and 60° in longitude (estimated at 40°N from the 5120 km actual width in plane geometry) on a Cartesian beta plane centered at 40°N, 3800 m deep. We conducted a series of experiments with increasing resolution from around 85-km horizontal resolution (59 × 54 grid points) and 20 levels, down to 10-km resolution (512 × 448 grid points) and 40 levels. The vertical grid spacing decreases from 841 (447) m at the bottom to 13 (6) m at the surface for the 20 (40) levels case. Temperature is the only active tracer related with density through a linear equation of state (the thermal expansion coefficient is $0.28\,\mathrm{kg\,m^{-3}\,K^{-1}}$). The forcing consists of surface heat flux prescribed as a linear function of latitude varying from $50\,\mathrm{W\,m^{-2}}$ at 20°N to $-50\,\mathrm{W\,m^{-2}}$ at 60°N. There is no wind forcing. The initial temperature is uniformly 4°C. The model is integrated for 2000 yr at 85- and 40-km resolution, 1000 yr at 20 km, and 500 yr at 10 km. The reference simulation uses 10^{-4} (10^{-3}) $\mathrm{m^2\,s^{-1}}$ vertical mixing for the tracer (momentum). Sensitivity experiments consist in varying the vertical mixing rate for temperature down to 3×10^{-5} and $10^{-5}\,\mathrm{m^2\,s^{-1}}$ (keeping the momentum vertical viscosity coefficient unchanged). Bottom drag is linear, with a coefficient of $3 \times 10^{-4}\,\mathrm{m\,s^{-1}}$.

This temperature vertical eddy diffusivity (K_V) along with the surface forcing drives a meridional overturning circulation (MOC), for which a scaling law has been proposed specifically for prescribed surface buoyancy flux with no wind as MOC strength $\propto K_V^{1/2}$ (Huang and Chou 1994; Park and Bryan 2000). The range of values explored for the vertical mixing certainly covers the range of observational estimates, but not their spatial variations (Polzin et al. 1997). Given the size of our single-hemisphere basin, deep-water formation in the north is only balanced by upwelling over a rather limited area; hence, the intensity of the overturning is much smaller in our simulations than would be expected in a bihemispheric or global configuration.

The 85-km experiment uses 700 (5×10^4) $\mathrm{m^2\,s^{-1}}$ horizontal mixing (K_H) for the tracer (momentum), whereas at higher resolution, no explicit values are prescribed and implicit mixing is controlled by the advection scheme. These explicit values are necessary at the lowest resolution to remove gridpoint noise that develops on the C grid, apparently because of the averaging of the velocities in the Coriolis term (Adcroft et al. 1999). These somehow "noisy" experiments with no explicit mixing are referred to as $K_H = 0$ but are not analyzed any further; they are the only ones that do not show smooth multidecadal oscillations but chaotic time series (Fig. 1, left). We use no-slip lateral boundary

conditions, but the use of free slip has no significant influence on the variability (Huck et al. 1999a).

3. The mean state

All the experiments for the various resolutions and vertical diffusivity values are summarized in Fig. 2a through the mean strength and variability of the overturning cell. In the absence of wind forcing and bottom topography, we would expect the vertically integrated velocities to almost cancel—only bottom friction and nonlinear advection terms drive a barotropic flow that usually remains weak, except in the turbulent western boundary current (WBC) detachment region. The overturning is then a good measure of the intensity of both the horizontal and vertical baroclinic circulation. The mean overturning varies at first order with the vertical mixing rate and only slightly with the horizontal resolution.

These series of experiments allow us to briefly check the validity of the scaling law proposed for the overturning as a function of the vertical mixing (K_V) under prescribed surface buoyancy flux (and no wind forcing): $\mathrm{MOC} \propto K_V^{1/2}$ (Huang and Chou 1994). Note that this differs from the one proposed under restoring surface boundary conditions (Welander 1986; Park and Bryan 2000), where $\mathrm{MOC} \propto K_V^{2/3}$. A linear regression of the mean overturning as a function of the vertical mixing, both in logarithms, for each resolution, strongly supports the ½ power law: slopes vary from 0.46 to 0.49, except for the lowest-resolution case (0.38)—yet each fit is computed over only three values of vertical mixing.

The latitude–depth structure of the mean meridional overturning streamfunction is shown by the contours in Fig. 3. As the strength of the mean MOC increases with vertical mixing, the location of the maximum overturning gets deeper, along with the thermocline depth. The range of temperature variations is forced at the surface through the prescribed differential heat flux. When vertical mixing is increased, these temperature variations penetrate deeper in the water column and drive the upper-layer velocities over a larger thickness, as discussed in detail in Bryan (1987) and Zhang et al. (1992), for instance. Since the barotropic flow almost vanishes over the largest fraction of the basin (except for the inertial WBC), the deep circulation must be the opposite of the upper circulation, and the depth of the velocity reversal corresponds to the maximum of the overturning streamfunction. This explains why the location of the maximum overturning gets deeper with increasing mixing, from 150 m for $10^{-5}\,\mathrm{m^2\,s^{-1}}$ to more than 600 m for $10^{-4}\,\mathrm{m^2\,s^{-1}}$ in the eddy-resolving experiments (the MOC maximum is more than twice as deep at 85-km resolution).

The amplitude of the mean overturning is surprisingly insensitive to the increase of the horizontal resolution,

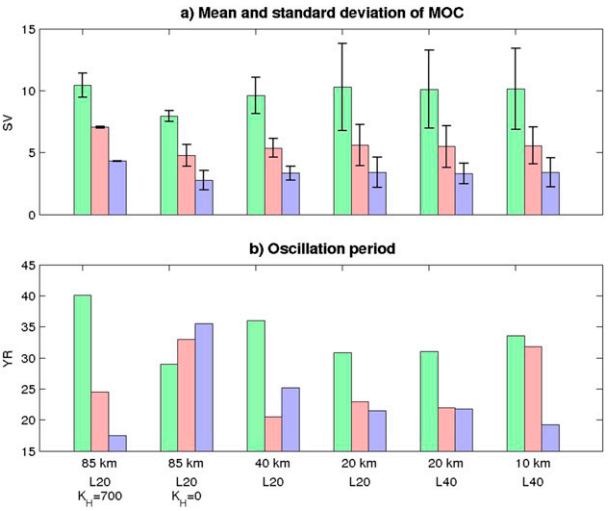

FIG. 2. (a) Meridional overturning streamfunction amplitude and variability (mean and standard deviation in Sv computed from annual-mean fields) for the 85-, 40-, 20-, and 10-km resolution experiments (with various numbers of vertical levels, L20 or L40), depending on the vertical diffusivity coefficient: 10^{-4} (green), 3×10^{-5} (red), and $10^{-5}\,\mathrm{m^2\,s^{-1}}$ (blue). Oscillations appear more robust at low vertical diffusivity and overturning with resolved eddy turbulence than without. (b) Oscillation period (yr) for all the experiments based on SST (0–100 m) and MOC time series. Oscillations sometimes occur as a superposition of 2 frequencies: only the largest amplitude period is then shown.

especially compared to the large variations in the mean temperature field, as shown, for instance, in sea surface temperature (Fig. 4, contours). The mean circulation associated geostrophically with these patterns changes dramatically from 85- to 40-km resolution, as the WBC shifts from a viscous laminar regime all along the western and northern boundaries to a turbulent regime where zonal jets separate chaotically from the coast farther south (~45°N) as the resolution increases. At the lowest resolution, the upper circulation consists in a single anticyclonic subtropical gyre, but as eddies set in, a narrow cyclonic subpolar gyre develops along the northern boundary (as indicated by the mean SSH contours in Fig. 5, left column). The geostrophic scaling of the MOC basically applies to the zonal velocity through surface-forced meridional density gradients, whereas the overturning circulation is essentially fed by the meridional WBC, such that the link between the zonal flow and the WBC remains tight independently of the horizontal reorganization of the upper circulation with varying resolution (Huck et al. 1999b).

4. The mesoscale turbulence

There are several ways to quantify the level of mesoscale activity in our simulations. Following the observation of sea level anomalies from satellite altimetry, one can estimate the standard deviation of sea surface

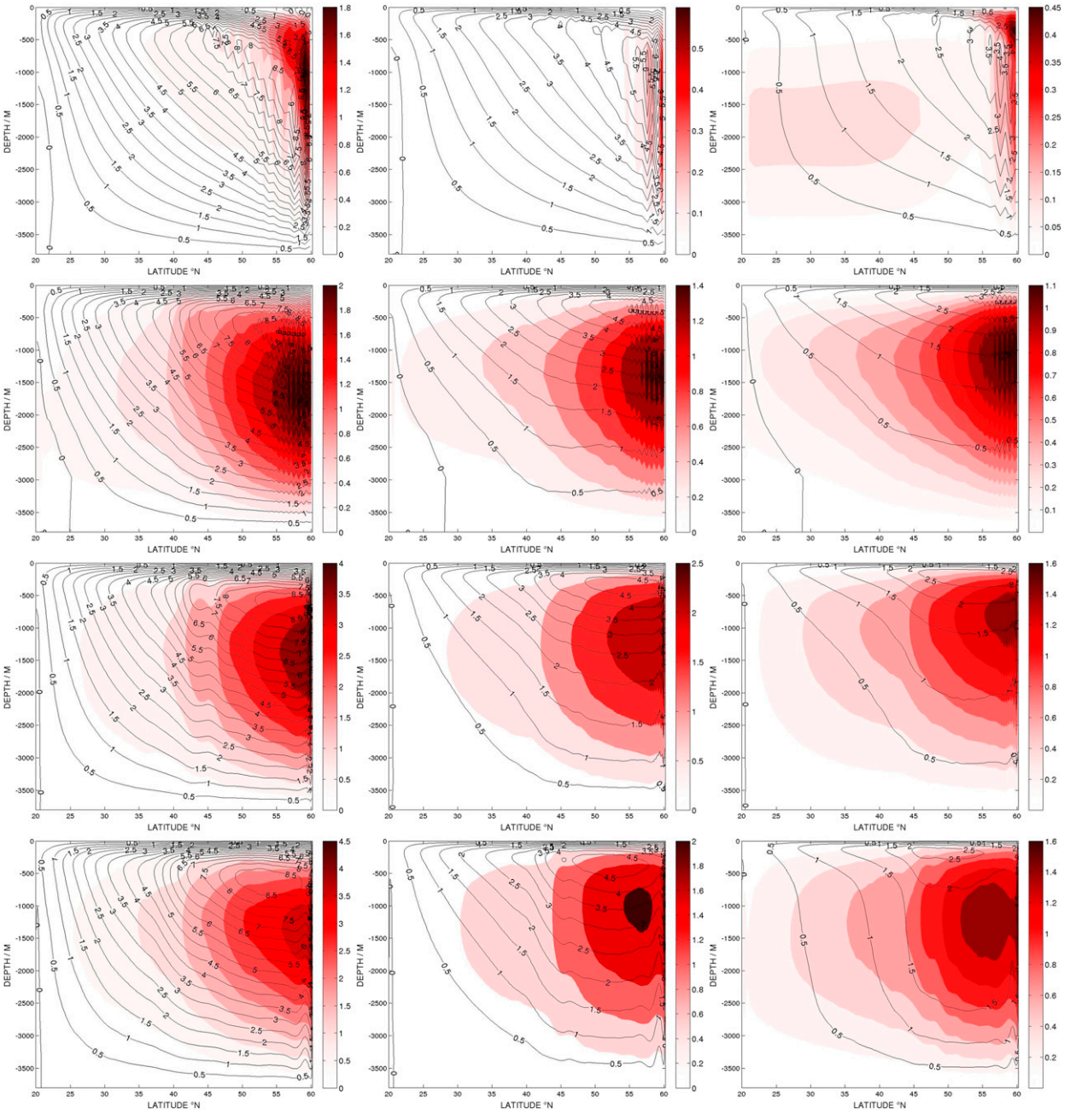

FIG. 3. MOC mean (contours) and standard deviation (color) for the (top to bottom) 85-, 40-, 20-, and 10-km resolution experiments for K_V = (left) 10^{-4}, (middle) 3×10^{-5}, and (right) $10^{-5}\,\mathrm{m^2\,s^{-1}}$, based on annual-mean fields (Sv). Note the color scale varies between the experiments. The mean overturning shows significant changes from the 85- to 40-km resolution, but much less for increasing resolution.

height (SSH). But one can also compute the turbulent kinetic energy from the velocity field. In all cases, it would be convenient to separate the short-term variations due to the mesoscale turbulence from the long-term variations associated with the multidecadal oscillations. This is done by decomposing the various fields in their low-frequency variations (noted with a superscript LF) defined as annually averaged values and the residual high-frequency variations (noted with a superscript HF) computed from monthly snapshots; for instance for sea surface height,

$$\mathrm{SSH}(x,y,t) = \mathrm{SSH}^{\mathrm{LF}}(x,y,t) + \mathrm{SSH}^{\mathrm{HF}}(x,y,t),$$

$$\text{with} \quad \mathrm{SSH}^{\mathrm{LF}}(x,y,t) = \int_{t-0.5\,\mathrm{yr}}^{t+0.5\,\mathrm{yr}} \mathrm{SSH}(x,y,t')\,dt'.$$

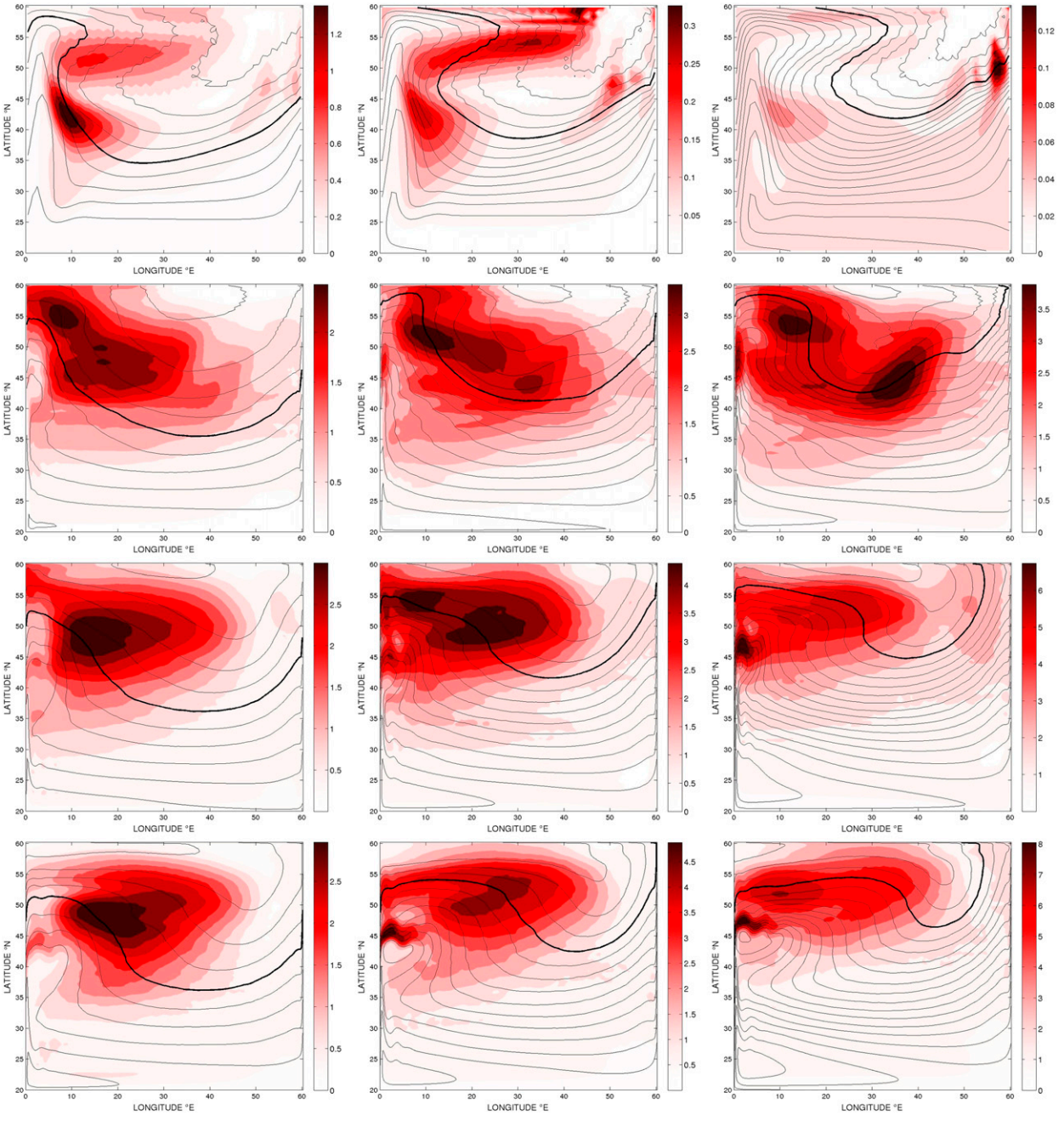

FIG. 4. SST (0–100 m) mean (contours every 2°C, bold is 12°C) and standard deviation (color; °C) for the (top to bottom) 85-, 40-, 20-, and 10-km resolution experiments for K_V = (left) 10^{-4}, (middle) 3×10^{-5}, and (right) 10^{-5} m^2 s^{-1}, based on annual-mean fields. Note the color scale varies between the experiments. Even the mean temperature shows large changes with resolution.

Recalling there is no seasonal cycle in our idealized forcing, the annual frequency is simply chosen here as a convenient cutoff between the eddy time scale and the multidecadal period.

For the lower-resolution experiment, the mesoscale part of SSH variability (defined as the standard deviation of SSH^{HF}) is close to zero, and the lower-frequency pattern is clearly detached from the western boundary (Fig. 5). As soon as some mesoscale structures are present (40-km resolution and higher), the high-frequency variations of SSH are localized in the region where the western boundary current detaches from the coast, around 45°N, and its maximum values increase with the resolution: 25 cm at 40-km resolution, 36 cm at 20 km, and

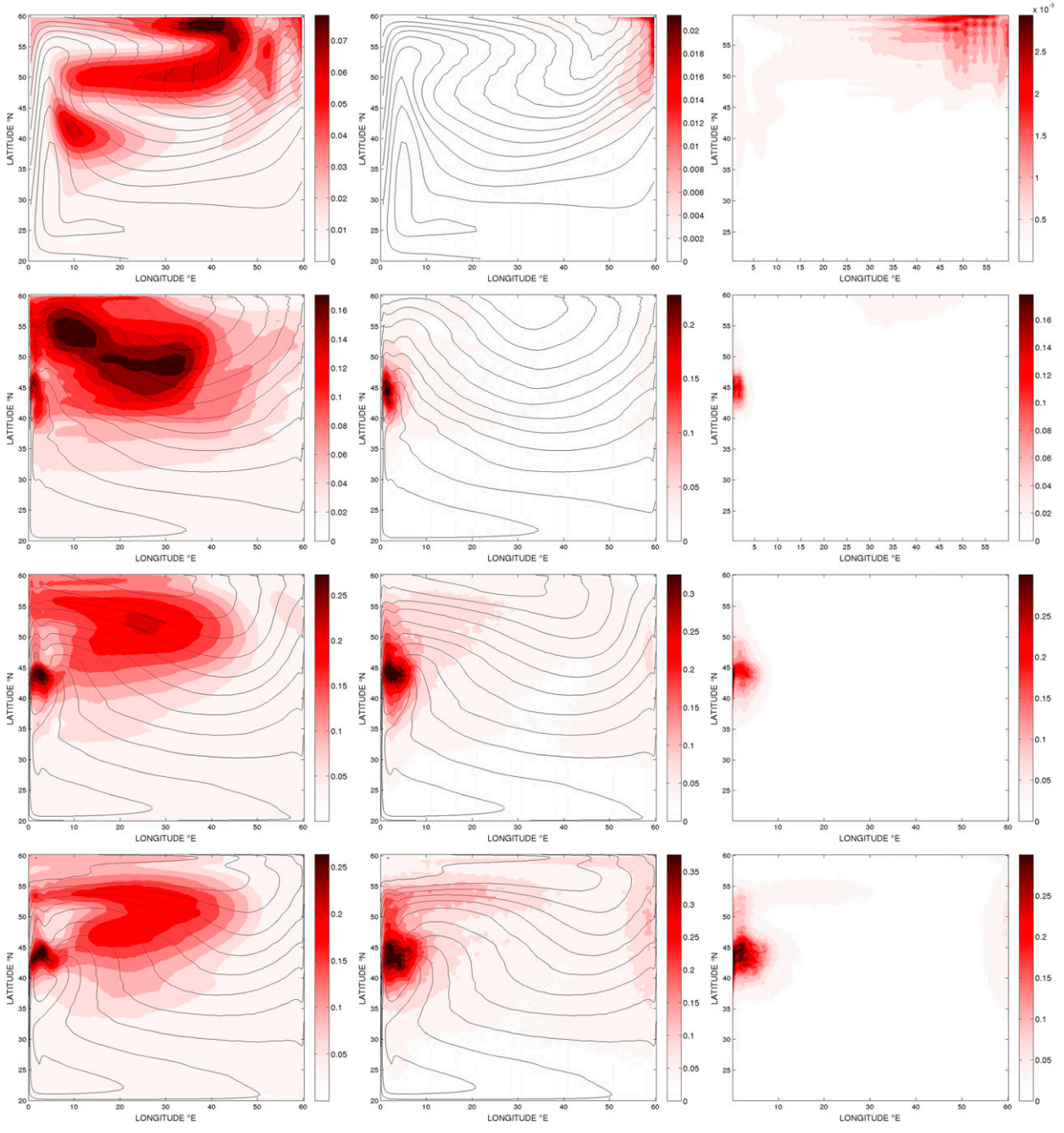

FIG. 5. Sea surface height mean (contours every 0.1 m) and standard deviation (color; m) for the (top to bottom) 85-, 40-, 20-, and 10-km resolution experiments for $K_V = 10^{-4}\,\mathrm{m^2\,s^{-1}}$, based on annual-mean fields for the (left) low frequency and on anomalies from annual running averages for the (middle) high frequency. (right) Surface eddy kinetic energy ($\mathrm{m^2\,s^{-2}}$) for the same experiments. Note the color scale varies between the experiments.

42 cm at 10 km for the high vertical mixing (Fig. 5, center panels). These maximum values also increase with the vertical mixing, through its major influence on the mean circulation. In comparison with altimetric observations of sea level anomalies (Stammer 1997, among many others), the amplitude of SSH variations suggests that the level of mesoscale turbulence is realistic for the 20- and 10-km resolution experiments. The low-frequency variability of SSH is estimated from the standard deviation of annually averaged fields ($\sigma_{\mathrm{SSH^{LF}}}$), although there is certainly some leakage from the high-frequency mesoscale signal (Fig. 5, left panels). The $\sigma_{\mathrm{SSH^{LF}}}$ pattern spreads over the northern

half of the basin, mostly in the northwest quarter, in close relation to temperature variability in the upper layer (Fig. 4, to be discussed in the next section). Except for the region of detachment of the WBC, $\sigma_{SSH^{LF}}$ amplitudes are around 20 cm and do not vary with the resolution. They result from the large-scale multidecadal variability of the temperature field. The patterns of SSH variability, their respective amplitude, and their sensitivity to the resolution clearly differ for the two frequency ranges. The high-frequency variations associated with mesoscale turbulence are localized in a small region close to the WBC detachment (a dynamical signal), whereas the low-frequency variations spread over the northwest quarter of the basin, in relation to multidecadal large-scale temperature variations (a thermodynamical steric signal).

To compare the mesoscale turbulence in our simulations with other numerical studies, we also computed the total kinetic energy (KE) field and its decomposition into the mean flow KE (MKE; computed from time-averaged velocities) and the remaining eddy field KE (EKE; also called turbulent kinetic energy). Whereas the MKE does not vary significantly with the resolution, the EKE keeps increasing, almost doubling each time the horizontal resolution is doubled. Its spatial pattern at the surface shows most of the energy in the region of WBC detachment, where values above $0.3\,m^2\,s^{-2}$ are obtained for the highest resolutions, even in the absence of wind forcing (Fig. 5, right panels). The patterns and their evolution with resolution correspond to the regions of large high-frequency SSH variability. With both metrics, the level of mesoscale activity appears comparable to observations and higher-resolution numerical experiments (Levy et al. 2010, 2014).

Given the few eddy-resolving numerical experiments with buoyancy forcing but no wind-forcing documented in the literature, it may be worth mentioning some singular aspects of the circulation related to the barotropic flow in our flat-bottom basin. In the absence of eddies (85-km resolution), the barotropic circulation results from the sole bottom friction term and remains weak. The time-mean anticyclonic barotropic streamfunction (BSF) peaks at 0.6 Sverdrups (Sv; $1\,Sv \equiv 10^6\,m^3\,s^{-1}$) in the northwest corner for the largest vertical mixing case (Fig. 6). As soon as eddies set in, nonlinear interactions feed a much more intense barotropic flow in the most energetic region, where the WBC detaches from the coast. The time-averaged BSF reaches values up to 25 Sv in an anticyclonic gyre located in the WBC between 40° and 45°N (where surface EKE and high-frequency SSH variability are at maximum in Fig. 5); elsewhere, values are of the order of several Sverdrups. BSF extrema based on annual-mean velocities easily reach 60 Sv at 40-km resolution and 80 Sv at 20- and 10-km resolution (for the larger vertical mixing cases). These very intense barotropic structures are the most prominent effect of the mesoscale eddy turbulence.

5. The multidecadal variability

As for simulations previously described in planetary geostrophic and primitive equations [Modular Ocean Model (MOM)] models, the integrations lead to spontaneous multidecadal variability on periods in the 20–40-yr range (Huck et al. 1999a, 2001), whatever the resolution, except for a single experiment at low resolution for the lowest vertical mixing case (where oscillations follow the initial energetic spinup but their amplitude slowly decays over several hundred years before a steady state is reached after 900 yr). Time series are shown in Fig. 1 for total KE, globally averaged SST (defined here as the upper 100 m), and MOC (defined as the maximum value of the meridional overturning streamfunction), the first being computed online on instantaneous fields at daily frequency, the latter two being computed from annually averaged temperature and velocity fields. It could appear surprising that total kinetic energy, which is mostly due to mesoscale eddies at higher resolution, varies on the decadal time scale in phase with the overturning and the basin-mean SST; in fact, the annual-mean circulation clearly evolves on the decadal time scale and controls the level of turbulent kinetic energy through baroclinic instability. For instance, considering altogether the 10-km resolution experiments for the three values of vertical mixing, the correlation between the time series of annually averaged total kinetic energy and MOC is 0.96; as discussed previously, in the absence of wind forcing, the MOC accurately measures the intensity of the large-scale circulation, and the total kinetic energy (mostly composed of eddy KE, for more than 93%) appears as a linear function of the MOC.

a. The overturning circulation

The amplitude of the low-frequency variations of the meridional overturning cell (computed every year from annually averaged meridional velocities) as a function of vertical diffusivity and horizontal resolution (Fig. 2a) shows the robustness and coherence of the interdecadal variability. In fact, the turbulent regime allows decadal oscillations to develop even at low vertical mixing (and overturning); that is not the case at low resolution, as already found in Huck et al. (1999a). Since the mean overturning is rather weaker at higher resolution compared to the 85-km case (Fig. 2a), there is no reason for the multidecadal mode to be more unstable in these cases. So, either the damping of the mode is lower because the resolved eddy diffusivity is lower than the one

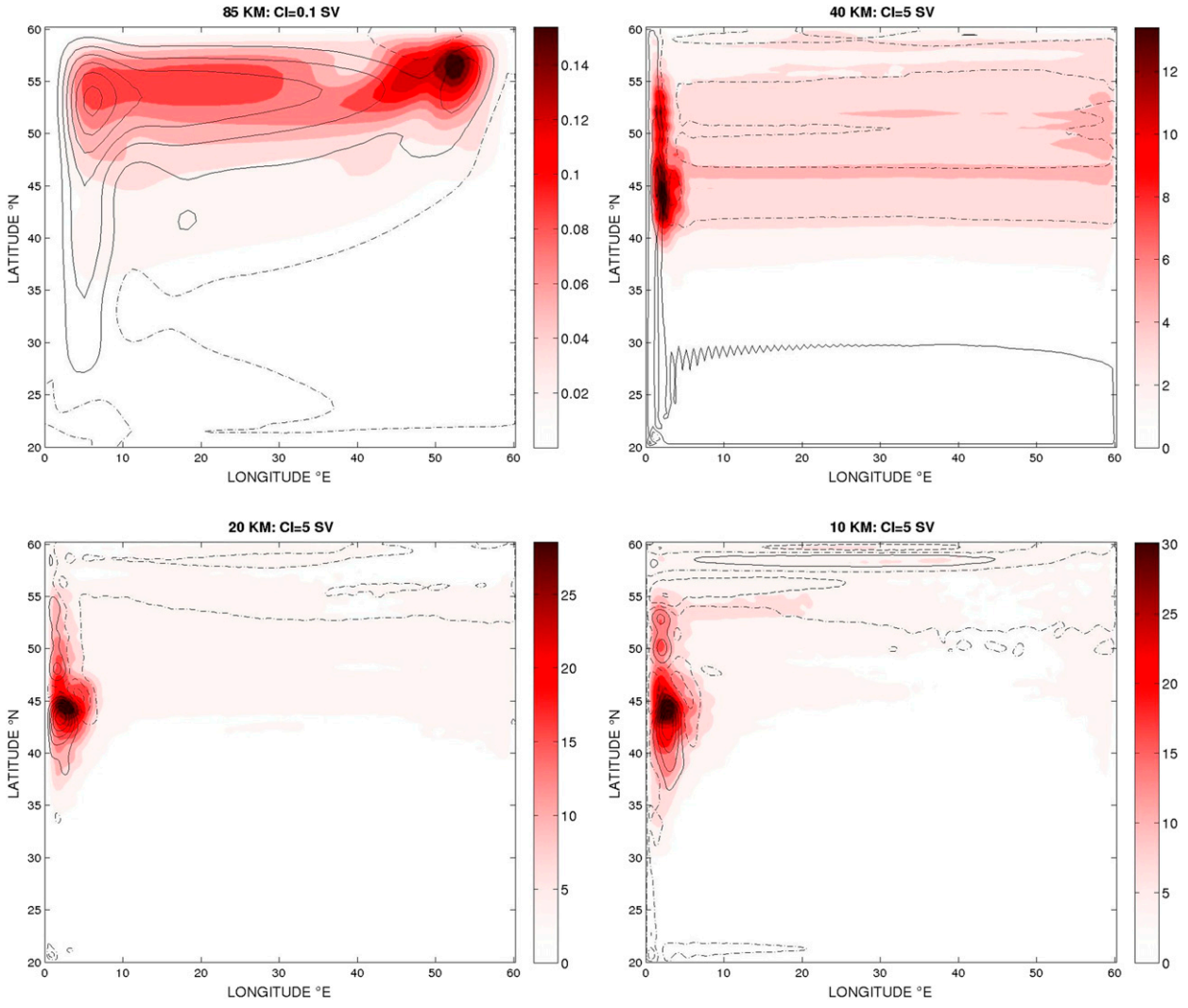

FIG. 6. Barotropic streamfunction mean (contours, solid for clockwise circulation, dashed for anticlockwise, dashed–dotted for zero) and standard deviation (color), computed from annually averaged velocities, for the (top left) 85-, (top right) 40-, (bottom left) 20-, and (bottom right) 10-km resolution experiments for $K_V = 10^{-4}\,\mathrm{m^2\,s^{-1}}$. The contour interval is 0.1 Sv for the 85-km resolution and 5 Sv otherwise. Note the color scale largely varies between experiments.

prescribed at the lowest resolution (the mean flow and shear is much weaker for the lowest vertical mixing case), the mode is damped but continually excited by the mesoscale turbulence that acts as an internal stochastic wavemaker (Frankcombe et al. 2009), or both factors contribute to sustain the oscillations.

The latitude–depth structure of the standard deviation of the (low frequency) meridional overturning streamfunction (Fig. 3) shows how the lower-resolution experiment fundamentally differs from the others; in the former, the variability is concentrated along the northern boundary, whereas in the latter cases, it spreads over a much broader range of latitude. This goes along with the changes in the upper-ocean circulation with increasing resolution, as the western boundary current shifts from a viscous to a turbulent regime and separates from the coast farther south.

b. *Temperature variability*

Spatial patterns of the standard deviation of SST (computed from annual averages over the upper 100 m) are shown in Fig. 4. Associated with the large changes in the mean circulation discussed previously, large changes occur in the variability patterns between 85- and 40-km resolution. But as the turbulent regime gets better resolved, one can see some convergence in the amplitude and structure of the SST mean and variability, as seen between the 20- and 10-km resolution. For the low-resolution experiments (85 and 40 km), some variability is localized along the northern boundary and has been

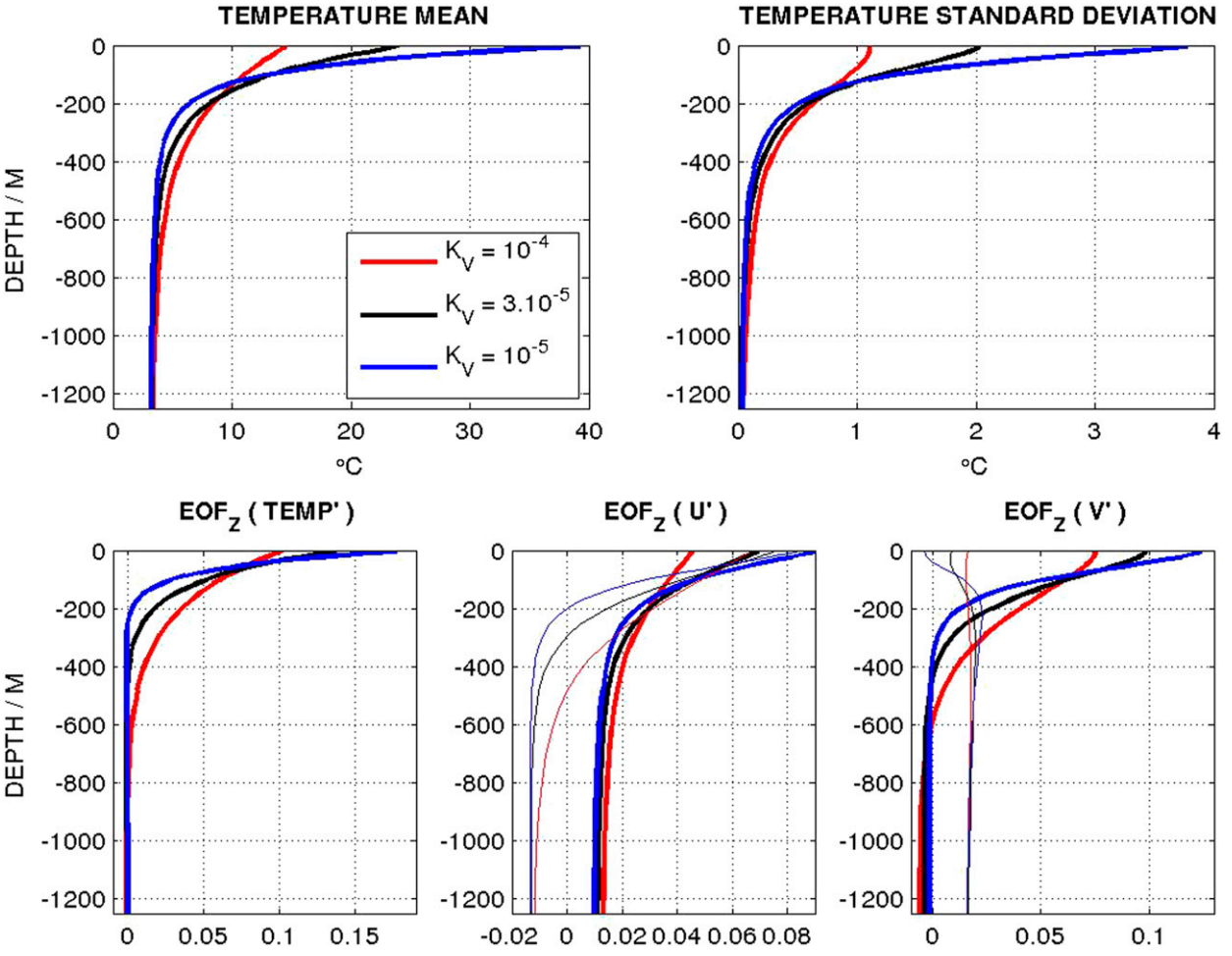

FIG. 7. Mean stratification and vertical structure of the perturbations as a function of vertical mixing for the 10-km resolution experiments. (top) Horizontally averaged temperature (left) mean and (right) standard deviation. (bottom) Leading EOFs of the temperature and velocity perturbations over the whole basin as functions of depth; only the first EOF is shown for temperature (representing 95 to 96% of the variance), and two EOFs are shown for the zonal and meridional velocities, representing respectively around 69% (bold) and 25% (thin) of the variance in all cases. Statistics are computed from annually averaged fields. The EOF decomposition for perturbations X' follows: $X'(x, y, z, t) = F(z)f(x, y, t)$. Note the depth scale extends only down to 1250 m, that is, around one-third of the total depth (3800 m), since the vertical structures vary very slightly below.

interpreted as the signature of Rossby waves. At higher resolution, the regions of large variability shift slightly southward, along with the front associated with the zonal jet in the eastward extension of the western boundary current (in analogy with the North Atlantic Drift).

Temperature variability decreases sharply with depth (Fig. 7), and below 1000 m it is localized along the northern boundary, mostly in the western half, and in the northwest corner. Below 2000 m, the maximum in the temperature variability coincides with the coldest mean temperature along the northern boundary, that is, the location of deep convection, where surface temperature anomalies can penetrate deeper layers. This location moves gradually from the northeast corner at 85-km resolution to the northwest corner at 10 km, as the narrow subpolar gyre builds up. Typical vertical structure of temperature anomalies does not usually change sign with depth (as shown by various empirical orthogonal functions analyses) and is more surface intensified with lower vertical mixing (Fig. 7). We have also investigated the vertical structure of the associated velocity anomalies through various EOF analyses, in the single vertical axis (see Fig. 7 lower-left panel and caption), or looking at vertical profiles of the three-dimensional EOFs. Typical vertical profiles for both zonal and meridional velocities for the 85- and 40-km resolution experiments (not shown) are similar to a first vertical baroclinic mode, with a zero moving shallower as vertical mixing is decreased, but with a stronger surface intensification compared to the pure stratification modes (as computed in the quasigeostrophic

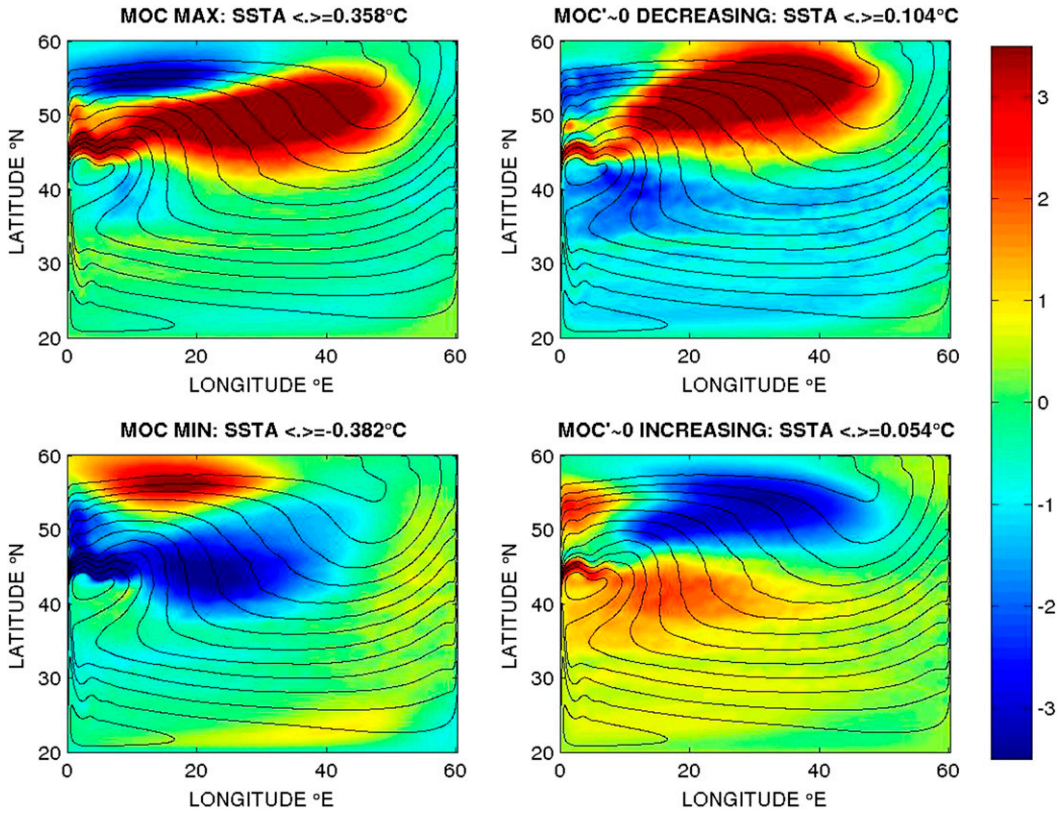

FIG. 8. SSTA (upper 100 m; °C) associated with four consecutive phases of the oscillations for the 10-km experiment with $K_V = 3 \times 10^{-5}\,\mathrm{m^2\,s^{-1}}$: (top left) when the MOC is at a maximum, (top right) when the MOC anomaly is small and decreasing, (bottom left) when the MOC is at a minimum, and (bottom right) when the MOC anomaly is small and increasing. The background mean SST appears as black contours and gives some insight on the upper circulation.

framework; see Huck et al. 2001). The barotropic component to the zonal velocity first EOF (Fig. 7, lower central panel) appears only at 20- and 10-km resolutions and may be associated with the development of zonal jets with increasing turbulence. Understanding the complex vertical structure of the perturbations and its spatial variations is beyond the scope of this study and is left for future work.

c. *Time evolution of temperature anomalies*

To provide some insights into the time evolution of temperature perturbations, we use the annual values of the MOC to compose averaged SST anomalies (SSTA) for periods when the MOC is at maximum (larger than the mean plus one standard deviation), when the MOC anomaly is close to zero and decreasing, when the MOC is at minimum (lower than the mean minus one standard deviation), and when the MOC anomaly is close to zero and increasing. This process allows the averaging together of from 10 to 45 annual-mean fields and filtering out some of the residual mesoscale turbulence. The large-scale propagation signal becomes much clearer as compared to each individual oscillation. For the 10-km resolution experiments, the SSTA patterns for the four phases of the oscillations are not altered by the vertical mixing rate, except that their maximum amplitude increases from typically 3° to 5°C as the vertical mixing is reduced and the anomalies are more trapped at the surface (Fig. 8). When the MOC is strong, a prominent positive SSTA is located at the exit of the western boundary current extending over most of the width of the basin, whereas a weaker negative SSTA remains in the northwest corner. As the MOC decreases, the positive anomaly slowly drifts northwestward, whereas a negative SSTA settles over the southern half of the basin. At the MOC minimum, the positive SSTA has reached the western boundary and occupies the northern part of the basin; the weaker MOC/WBC, associated with a reduced poleward heat transport, allows a large negative SSTA to grow over the center of the basin (its eastern extension is less pronounced than for the positive SSTA associated with strong MOC because in the

latter case the stronger WBC extends farther east). As the MOC increases, the positive SSTA disappears in the western boundary as the prominent negative SSTA grows and slowly drifts northwestward. In the meantime, positive SSTA start growing in the southern half of the basin as the WBC builds up. Similarity with the interdecadal oscillation described by Greatbatch and Zhang (1995, their Fig. 6) is striking, although the phase may be slightly shifted.

At depth, temperature variability is not as widespread as in the upper layers, and below 700 m, perturbations are localized along the northern boundary and in the northwest corner. The amplitude of the perturbations also decays regularly with depth. In general, perturbations propagate westward along the northern boundary and southward upon their arrival on the western boundary; it is difficult to track them farther south once they have reached the turbulent region of detachment of the WBC. From Hövmoller diagrams along the northern boundaries (not shown), deep anomalies follow closely the upper anomalies during their westward propagation (Fig. 8), but with an eastward shift close to $\pi/2$ that has been previously interpreted as a signature of baroclinic instability (Colin de Verdière and Huck 1999; Arzel et al. 2006). The westward propagation is ubiquitous in the western half along the northern boundary, at all depths. This has been interpreted as baroclinic Rossby waves, although the accurate rationalization of their propagation speed remains difficult because of strong wave–mean flow interactions. In contrast, the westward propagation is not ubiquitous in the eastern half of the northern boundary. In some experiments, the upper-layer anomalies that grow in the extension of the WBC may reach the northern boundary in the center of the basin—in such case, deep anomalies show propagation in both directions, westward to the west of this point and eastward to the east, where they decay before reaching the eastern boundary.

Another way to look at the coupling between upper and lower layers is through the mixed layer depth (MLD), which also shows clear westward propagation along the northern boundary. Spall (2008, and references therein) has shown a good correlation between the MOC intensity and the MLD averaged over about 1° of latitude all along the northern boundary in idealized geometry, eddy-resolving experiments forced by both heat fluxes and wind stress; this relationship holds in our experiments and is slightly better than the correlation with SST. However, because the zonal velocities along the northern boundary are largely influenced by the overturning circulation in the absence of a wind-driven subpolar gyre, the MLD along the northern boundary is not as clearly influenced by the horizontal circulation.

6. The oscillation period

Just like in the observations, where the AMO may be more rigorously referred to as ''variability'' (AMV), some of our experiments do not show regular periodic monochromatic oscillations but more complex signals. In the latter case, we have estimated the most energetic period from the time series (MOC, SST, or KE) that showed the clearer signal. The actual or most energetic oscillation periods are summarized in Fig. 2b. For simplicity, we will refer to these values as the oscillation period in the following.

Periods vary from 18 to 40 yr, but more often gather around 22 and 33 yr. We exclude the low-resolution experiments with no explicit diffusivity because of the noise induced by the numerics. For large vertical mixing, the periods are all between 31 and 40 yr. For low vertical mixing, they are all between 17 and 25 yr. For intermediate vertical mixing, they are mostly in the 20–24-yr range except at the highest resolution where the period shifts to 32 yr. Overall, the oscillation period increases with the vertical diffusivity, in agreement with previous studies at low resolution for the thermally driven (Huck et al. 1999a) and salinity-driven (Huang and Chou 1994) circulations. As the vertical mixing increases, the stratification decreases, and the westward velocity of baroclinic waves is expected to decrease, such that their basin crossing time increases. Of course, this hand-waving argument neglects several aspects of the propagation that are difficult to scale with vertical mixing. The meridional gradient of temperature and density is certainly as important as the gradient of planetary vorticity for the westward propagation, as well as the influence of the mean circulation. However, we have checked that the first baroclinic Rossby radius of deformation (R_d) averaged over the whole basin area north of 50°N decreases from 12 km for the lowest mixing to 10 km for the highest. The associated reduction in baroclinic Rossby wave velocity (βR_d^2; where β is the meridional gradient of planetary vorticity) by 36% provides a reasonable quantitative estimate for the observed increase in the oscillation period.

The shift of the oscillation period from 22 yr at 20-km resolution to 32 yr at 10 km, for the intermediate value of vertical mixing, is worth investigating because these two experiments are otherwise very similar, both in terms of mean state and variability. As is often the case when the oscillations are not monochromatic, there are two oscillation frequencies that superpose with different amplitude. Hövmoller diagrams along the northern boundary (not shown) indicate that at 10-km resolution, temperature anomalies have the largest zonal wavelength (a zonal mode 1); a one-sign temperature anomaly usually occupies most of the basin width. The 20-km

resolution case is more complex: temperature anomalies of the same signs along the northern boundary are alternatively strong and weak at depth, whereas the associated anomalies in the upper layer appear in the center of the basin for the strong ones but only in the western corner for the weak ones. At all depths their zonal structure generally shows three nodes. Hence, we believe this experiment shows the superposition of two Rossby waves (zonal modes 1 and 2) propagating along the northern boundary and generating a more complex spectrum of variability with two main periods. The sustained higher-wavenumber Rossby mode at 20-km resolution may result from lower mesoscale eddy turbulence at 20 km compared to the 10-km experiment (as suggested by the standard deviation of sea surface height or surface eddy kinetic energy for instance).

At 10-km resolution for the high vertical diffusivity, the oscillations are quite regular with very similar amplitude and a period around 33.6 yr. As the vertical diffusivity decreases, the oscillations become less regular; for the intermediate diffusivity, the oscillations remain quite regular in terms of amplitude and period, although there is often some hiatus in the growing phase of the MOC. But for the lowest value of diffusivity, the oscillations amplitude is very irregular (varying by a factor of 5), and the period (varying almost by a factor of 2) appears to increase with the oscillation amplitude (period and amplitude are measured here between consecutive minima and maxima of the MOC). Obviously the stochastic excitation of the eddies may well have a role in sustaining the oscillations in that case.

7. Discussion

Resolving mesoscale eddies, hence introducing a small-scale high-frequency wavemaker, does not disturb the coherence of the large-scale multidecadal variability found in idealized geometry ocean models forced by prescribed surface heat flux, but rather makes the latter more robust to low values of eddy diffusivity and overturning. This behavior is somewhat unexpected since the variability is associated with the propagation of large-scale Rossby waves in the poleward region of the basin, which could eventually not maintain coherent wave fronts in the presence of mesoscale turbulence, as suggested by LaCasce and Pedlosky (2004) and Isachsen et al. (2007). Looking at the evolution of SST anomalies in our high-resolution simulations, it appears that the variability is not initiated as wave fronts emanating from the eastern boundary and propagating westward mostly, we believe, because the proximity of the western boundary region makes changes in the overturning/WBC transport of first-order importance for initiating and shaping these anomalies. Warm anomalies develop with increasing MOC/WBC transport and vice versa (Fig. 8). Now examining closely the contours of these large-scale SST anomalies, which could be interpreted as Rossby wave fronts, along their usually westward propagation, it appears that mesoscale instabilities do grow on their periphery, but their growth remains sufficiently small that the large-scale contours maintain their coherence by the time they reach the western boundary (a few to 10 yr). LaCasce and Pedlosky (2004) and Isachsen et al. (2007) suggest to compare the basin crossing time for the baroclinic Rossby waves [$T_R = L_B/(\beta L_D^2)$, with L_B the basin zonal extent] to the unstable growth time of baroclinic instability at the internal deformation radius scale L_D ($T_g = L_D/U$, with U the typical shear velocity). Computing this ratio $Z = T_R/T_g = UL_B/(\beta L_D^3)$ for our simulations leads to values of order 1000, depending mainly on the zonal velocity shear considered (decadal means are close to 0.01–0.02 m s^{-1} but annual-mean fields are closer to 0.05–0.1 m s^{-1}).

There may be an order of magnitude overestimation of the baroclinic growth rate because of the implicit biharmonic viscosity and diffusivity associated with the advection schemes and the insufficient resolution that hardly resolves the first baroclinic radius of deformation. Another half order of magnitude overestimation may come from the fact that waves are not initiated at the eastern boundary but from variations of the MOC through the WBC and propagate westward over shorter distances. In addition the westward propagation may not rely on the gradient of planetary vorticity β but rather on the slope of the thermocline, which significantly affects the velocity. Nevertheless, this is still not enough to justify their coherent propagation according to these criteria. Maybe the evolution of the mean fields on which the mesoscale instability grows is to be invoked to reduce the growth rate or the stabilizing effect of beta, but also the fact that on time scales of years to decades eddies are no longer in a linear growing regime but have equilibrated and feed the large scales through the inverse cascade should be invoked. In fact the major interactions involved in our large-scale anomalies' instability are from baroclinic modes, so that the barotropic–baroclinic wave interactions considered in the LaCasce and Pedlosky (2004) two-layer model are not relevant here; only the primitive equation simulations of Isachsen et al. (2007) are in the same regime, although there is no mean flow. All these arguments remain very speculative, but the fully nonlinear regime of our simulations and the retroactions of the Rossby waves with the mean flow may be the key differences.

The oscillations that develop in our forced eddy-resolving simulations result from the constructive

interactions of three processes: 1) the large-scale Rossby waves propagation, 2) their fully developed baroclinic instabilities that feedback on large scales through the inverse cascade, and 3) their feedback on the mean flow. As such, their stability obviously differs from the stability of an imposed Rossby wave pattern with no mean flow. Depending on the amplitude of the mean circulation and its large-scale stability, the mesoscale eddies may have a stabilizing influence on unstable modes by releasing the available potential energy of the Rossby waves' fronts (as captured by the eddy diffusivity used at low resolution) or a destabilizing influence for stable modes through the generation of stochastic noise. So the major result from this series of experiments is the robustness of the large-scale modes against resolved baroclinic eddies, although it is not obvious why they are so robust.

8. Conclusions and perspectives

The series of numerical experiments reported here confirm the robustness and ubiquitous nature of the mechanism of multidecadal variability of the thermally driven overturning circulation found at low non-eddy-permitting resolution, at least with respect to the mesoscale turbulence. The patterns of the variability are strongly affected by the resolution of the mesoscale eddies and their rectification on the mean flow. The oscillation period is mostly unchanged with varying resolution, but generally increases when vertical mixing is increased. Under prescribed surface heat fluxes and with no wind forcing, the mean overturning circulation scales as the square root of the vertical mixing, quite independently of the resolution. This suggests that the nonlinear rectification of the mean overturning by the eddy forcing remains quite limited, despite a significant influence on the mean upper circulation (as found in wind-driven simulations). The level of mesoscale turbulence achieved at 20- and 10-km resolutions is comparable with altimetric observations in terms of SSH variability or surface eddy kinetic energy. We found that for a given horizontal resolution, the total kinetic energy, mostly contained at the most energetic mesoscale, evolves as a linear function of the large-scale circulation as measured by the meridional overturning circulation. This confirms the efficiency of baroclinic instability to convert the large-scale potential energy reservoir into eddy kinetic energy on time scales much shorter than a year. Overall, resolving the mesoscale turbulence extends the range of vertical mixing that allows multidecadal oscillations, either because the associated eddy diffusivity is lower than that prescribed at low resolution and induces less damping on the large scales, because the eddies play the role of a stochastic process that sustains the oscillation even if they are damped (Frankcombe et al. 2009; Sévellec et al. 2009), or both (more extensive analysis would be necessary to determine the exact cause). We have not discussed further the mechanism of these oscillations because our results do not challenge the interpretation that has been proposed before, as illustrated in Fig. 8. A large-scale baroclinic Rossby wave propagates westward along the northern boundary and feedbacks on the mean circulation upon reaching the western boundary, its vertical tilt with depth suggesting it is extracting energy from the mean density field.

Work will be pursued to examine if this genuine intrinsic variability of the ocean thermohaline circulation may have a role in the observed North Atlantic climate variability on decadal to multidecadal periods. For instance, bottom topography has been suggested as playing a damping role on such variability (Winton 1997). The wind forcing would have to be considered to obtain a more realistic circulation, but will trigger its own type of interannual variability when eddies are resolved (Hazeleger and Drijfhout 2000; Berloff et al. 2007b). The simulations reported here do not allow a reasonable comparison of the oscillations with observations for obvious reasons (idealized forcing and geometry), but capture the essential processes leading to spontaneous multidecadal variability. In the next paragraphs, we report briefly on published studies that give some hints on what could be the period and structure of these oscillations in more realistic configurations.

Sévellec and Fedorov (2013) recently exhibited the leading eigenmode in a realistic low-resolution global ocean model [Ocean Parallelise (OPA)/Nucleus for European Modeling of the Ocean (NEMO) ORCA 2°]. The mechanism they propose for explaining this damped oscillation with a 24-yr period also relies on a zonally propagating Rossby wave, not along the poleward boundary as in idealized setup, but rather along the North Atlantic Current front. A 20-yr sustained mode in the same ocean model coupled to atmospheric, land, and ice models (Escudier et al. 2013) bears some striking resemblance with the damped ocean mode. In idealized configurations including a double gyre wind forcing, the main variability region also appears to shift from the northern region to the intergyre (T. Huck, unpublished work 2014). This is already what happens here when the SST variability shifts from along the northern boundary at low resolution to slightly southward regions at higher resolution (Fig. 4), following the main front associated with the extension of the western boundary current after its detachment.

The use of prescribed surface heat flux in our series of experiments probably amplifies the SST signature of the

oscillations: what would happen with more realistic air–sea interactions? A similar oscillation mechanism has been recently recalled to explain oscillations in idealized coupled models. In the University of Victoria (UVic) coupled model where the atmosphere is an Energy–Moisture Balance Model, Arzel et al. (2012) describe strong interdecadal oscillations (period around 35 yr) in the North Atlantic during the warm interstadial phases of millennial oscillations. In a double Drake aquaplanet configuration of the Massachusetts Institute of Technology (MIT) coupled GCM, Buckley et al. (2012) show a 30-yr oscillation in the small (North Atlantic like) basin with two potential regions of variance growth on the eastern and western boundaries, promoting the role of unstable Rossby waves in the northern part of the basin. This analysis has been extended to the oscillations in more realistic coupled simulations, namely, with National Center for Atmospheric Research (NCAR) Community Climate System Model, version 3 (CCSM3), and the Geophysical Fluid Dynamics Laboratory (GFDL) Climate Model, version 2.1 (CM2.1), highlighting the role of upper-ocean density anomalies propagating around the subpolar gyre and geostrophically affecting the AMOC when arriving in the northwest region (Tulloch and Marshall 2012). In conclusion, this intrinsic mechanism of oceanic low-frequency variability remains a paradigm for the multidecadal climate variability found in coupled models and observed in the North Atlantic (Frankcombe and Dijkstra 2009; Chylek et al. 2011).

Acknowledgments. The publication of this article is financed by the Centre National d'Etudes Spatiales (CNES) through the CHAOCEAN project, coordinated in LGGE, Grenoble, and supported by the Ocean Surface Topography Science Team (OST/ST). This work is also a contribution to the Ti Ammo project funded through the French CNRS/INSU/LEFE/EVE program. Thanks to the ROMS–AGRIF community that make freely available their models and documentations, and, namely, to Gildas Cambon, Xavier Capet, Florian Lemarié, Patrick Marchesiello, and Pierrick Penven for their help. Wise comments and suggestions from Alain Colin de Verdière and two reviewers are gratefully acknowledged. Computational resources were provided by the Pôle de Calcul Intensif pour la Mer at Ifremer, Brest, France.

REFERENCES

Adcroft, A., C. Hill, and J. Marshall, 1999: A new treatment of the Coriolis terms in C-grid models at both high and low resolutions. *Mon. Wea. Rev.,* **127,** 1928–1936, doi:10.1175/1520-0493(1999)127<1928:ANTOTC>2.0.CO;2.

Arzel, O., T. Huck, and A. Colin de Verdière, 2006: The different nature of the interdecadal variability of the thermohaline circulation under mixed and flux boundary conditions. *J. Phys. Oceanogr.,* **36,** 1703–1718, doi:10.1175/JPO2938.1.

——, M. H. England, A. Colin de Verdière, and T. Huck, 2012: Abrupt millennial variability and interdecadal-interstadial oscillations in a global coupled model: Sensitivity to the background climate state. *Climate Dyn.,* **39,** 259–275, doi:10.1007/s00382-011-1117-y.

Ba, J., N. S. Keenlyside, W. Park, M. Latif, E. Hawkins, and H. Ding, 2013: A mechanism for Atlantic multidecadal variability in the Kiel Climate Model. *Climate Dyn.,* **41,** 2133–2144, doi:10.1007/s00382-012-1633-4.

Berloff, P., W. Dewar, S. Kravtsov, and J. McWilliams, 2007a: Ocean eddy dynamics in a coupled ocean–atmosphere model. *J. Phys. Oceanogr.,* **37,** 1103–1121, doi:10.1175/JPO3041.1.

——, A. Hogg, and W. Dewar, 2007b: The turbulent oscillator: A mechanism of low-frequency variability of the wind-driven ocean gyres. *J. Phys. Oceanogr.,* **37,** 2363–2386, doi:10.1175/JPO3118.1.

Bryan, F., 1987: Parameter sensitivity of primitive equation ocean general circulation models. *J. Phys. Oceanogr.,* **17,** 970–985, doi:10.1175/1520-0485(1987)017<0970:PSOPEO>2.0.CO;2.

——, G. Danabasoglu, N. Nakashiki, Y. Yoshida, D.-H. Kim, J. Tsutsui, and S. C. Doney, 2006: Response of the North Atlantic thermohaline circulation and ventilation to increasing carbon dioxide in CCSM3. *J. Climate,* **19,** 2382–2397, doi:10.1175/JCLI3757.1.

Buckley, M. W., D. Ferreira, J.-M. Campin, J. Marshall, and R. Tulloch, 2012: On the relationship between decadal buoyancy anomalies and variability of the Atlantic meridional overturning circulation. *J. Climate,* **25,** 8009–8030, doi:10.1175/JCLI-D-11-00505.1.

Cessi, P., and F. Paparella, 2001: Excitation of basin modes by ocean-atmosphere coupling. *Geophys. Res. Lett.,* **28,** 2437–2440, doi:10.1029/2000GL012660.

Charney, J. G., 1947: The dynamics of long waves in a baroclinic westerly current. *J. Meteor.,* **4,** 135–162, doi:10.1175/1520-0469(1947)004<0136:TDOLWI>2.0.CO;2.

Chylek, P., C. K. Folland, H. A. Dijkstra, G. Lesins, and M. K. Dubey, 2011: Ice-core data evidence for a prominent near 20 year time-scale of the Atlantic multidecadal oscillation. *Geophys. Res. Lett.,* **38,** L13704, doi:10.1029/2011GL047501.

Colin de Verdière, A., and T. Huck, 1999: Baroclinic instability: An oceanic wavemaker for interdecadal variability. *J. Phys. Oceanogr.,* **29,** 893–910, doi:10.1175/1520-0485(1999)029<0893:BIAOWF>2.0.CO;2.

Delworth, T. L., and R. J. Greatbatch, 2000: Multidecadal thermohaline circulation variability driven by atmospheric surface flux forcing. *J. Climate,* **13,** 1481–1495, doi:10.1175/1520-0442(2000)013<1481:MTCVDB>2.0.CO;2.

——, and M. E. Mann, 2000: Observed and simulated multidecadal variability in the Northern Hemisphere. *Climate Dyn.,* **16,** 661–676, doi:10.1007/s003820000075.

——, S. Manabe, and R. J. Stouffer, 1993: Interdecadal variations of the thermohaline circulation in a coupled ocean–atmosphere model. *J. Climate,* **6,** 1993–2011, doi:10.1175/1520-0442(1993)006<1993:IVOTTC>2.0.CO;2.

——, R. Zhang, and M. E. Mann, 2007: Decadal to centennial variability of the Atlantic from observations and models. *Ocean Circulation: Mechanisms and Impacts, Geophys. Monogr.,* Vol. 173, Amer. Geophys. Union, 131–148.

Deser, C., and M. L. Blackmon, 1993: Surface climate variation over the North Atlantic Ocean during winter: 1900–1989.

J. Climate, **6,** 1743–1753, doi:10.1175/1520-0442(1993)006<1743:SCVOTN>2.0.CO;2.

Dijkstra, H. A., and M. Ghil, 2005: Low-frequency variability of the large-scale ocean circulation: A dynamical systems approach. *Rev. Geophys.,* **43,** RG3002, doi:10.1029/2002RG000122.

Eady, E. T., 1949: Long waves and cyclone waves. *Tellus,* **1,** 33–52, doi:10.1111/j.2153-3490.1949.tb01265.x.

Eden, C., and T. Jung, 2001: North Atlantic interdecadal variability: Oceanic response to the North Atlantic Oscillation (1865–1997). *J. Climate,* **14,** 676–691, doi:10.1175/1520-0442(2001)014<0676:NAIVOR>2.0.CO;2.

Escudier, R., J. Mignot, and D. Swingedouw, 2013: A 20-yr coupled ocean-sea ice-atmosphere variability mode in the North Atlantic in an AOGCM. *Climate Dyn.,* **40,** 619–636, doi:10.1007/s00382-012-1402-4.

Frankcombe, L. M., and H. A. Dijkstra, 2009: Coherent multidecadal variability in North Atlantic sea level. *Geophys. Res. Lett.,* **36,** L15604, doi:10.1029/2009GL039455.

——, ——, and A. von der Heydt, 2009: Noise-induced multidecadal variability in the North Atlantic: Excitation of normal modes. *J. Phys. Oceanogr.,* **39,** 220–233, doi:10.1175/2008JPO3951.1.

Greatbatch, R. J., and S. Zhang, 1995: An interdecadal oscillation in an idealized ocean basin forced by constant heat fluxes. *J. Climate,* **8,** 81–91, doi:10.1175/1520-0442(1995)008<0081:AIOIAI>2.0.CO;2.

Griffies, S. M., and E. Tziperman, 1995: A linear thermohaline oscillator driven by stochastic atmospheric forcing. *J. Climate,* **8,** 2440–2453, doi:10.1175/1520-0442(1995)008<2440:ALTODB>2.0.CO;2.

Hazeleger, W., and S. S. Drijfhout, 2000: A model study on internally generated variability in subtropical mode water formation. *J. Geophys. Res.,* **105,** 13 965–13 979, doi:10.1029/2000JC900041.

Hodson, D. L. R., and R. T. Sutton, 2012: The impact of resolution on the adjustment and decadal variability of the Atlantic meridional overturning circulation in a coupled climate model. *Climate Dyn.,* **39,** 3057–3073, doi:10.1007/s00382-012-1309-0.

Huang, R. X., and R. L. Chou, 1994: Parameter sensitivity study of the saline circulation. *Climate Dyn.,* **9,** 391–409, doi:10.1007/BF00207934.

Huck, T., and G. K. Vallis, 2001: Linear stability analysis of three-dimensional thermally-driven ocean circulation: Application to interdecadal oscillations. *Tellus,* **53A,** 526–545, doi:10.1111/j.1600-0870.2001.00526.x.

——, A. Colin de Verdière, and A. J. Weaver, 1999a: Interdecadal variability of the thermohaline circulation in box-ocean models forced by fixed surface fluxes. *J. Phys. Oceanogr.,* **29,** 865–892, doi:10.1175/1520-0485(1999)029<0865:IVOTTC>2.0.CO;2.

——, A. J. Weaver, and A. Colin de Verdière, 1999b: On the influence of the parameterization of lateral boundary layers on the thermohaline circulation in coarse-resolution ocean models. *J. Mar. Res.,* **57,** 387–426, doi:10.1357/002224099764805138.

——, G. K. Vallis, and A. Colin de Verdière, 2001: On the robustness of the interdecadal modes of the thermohaline circulation. *J. Climate,* **14,** 940–963, doi:10.1175/1520-0442(2001)014<0940:OTROTI>2.0.CO;2.

Isachsen, P. E., J. H. LaCasce, and J. Pedlosky, 2007: Rossby wave instability and apparent phase speeds in large ocean basins. *J. Phys. Oceanogr.,* **37,** 1177–1191, doi:10.1175/JPO3054.1.

James, I. N., and P. M. James, 1989: Ultra-low-frequency variability in a simple atmospheric circulation model. *Nature,* **342,** 53–55, doi:10.1038/342053a0.

Knight, J. R., R. J. Allan, C. K. Folland, and M. E. Mann, 2005: A signature of persistent natural thermohaline circulation cycles in observed climate. *Geophys. Res. Lett.,* **32,** L20708, doi:10.1029/2005GL024233.

Kravtsov, S., P. Berloff, W. K. Dewar, M. Ghil, and J. C. McWilliams, 2006: Dynamical origin of low-frequency variability in a highly nonlinear midlatitude coupled model. *J. Climate,* **19,** 6391–6408, doi:10.1175/JCLI3976.1.

Kushnir, Y., 1994: Interdecadal variations in North Atlantic sea surface temperature and associated atmospheric conditions. *J. Climate,* **7,** 141–157, doi:10.1175/1520-0442(1994)007<0141:IVINAS>2.0.CO;2.

LaCasce, J. H., and J. Pedlosky, 2004: The instability of Rossby basin modes and the oceanic eddy field. *J. Phys. Oceanogr.,* **34,** 2027–2041, doi:10.1175/1520-0485(2004)034<2027:TIORBM>2.0.CO;2.

Levy, M., P. Klein, A.-M. Treguier, D. Iovino, G. Madec, S. Masson, and K. Takahashi, 2010: Modifications of gyre circulation by sub-mesoscale physics. *Ocean Modell.,* **34,** 1–15, doi:10.1016/j.ocemod.2010.04.001.

——, L. Resplandy, and M. Lengaigne, 2014: Oceanic mesoscale turbulence drives large biogeochemical interannual variability at middle and high latitudes. *Geophys. Res. Lett.,* **41,** 2467–2474, doi:10.1002/2014GL059608.

Marsh, R., B. A. de Cuevas, A. C. Coward, J. Jacquin, J. J.-M. Hirschi, Y. Aksenov, A. J. G. Nurser, and S. A. Josey, 2009: Recent changes in the North Atlantic circulation simulated with eddy-permitting and eddy-resolving ocean models. *Ocean Modell.,* **28,** 226–239, doi:10.1016/j.ocemod.2009.02.007.

Mecking, J., N. Keenlyside, and R. Greatbatch, 2014: Stochastically-forced multidecadal variability in the North Atlantic: A model study. *Climate Dyn.,* **43,** 271–288, doi:10.1007/s00382-013-1930-6.

Ollitrault, M., and A. Colin de Verdière, 2002: SOFAR floats reveal midlatitude intermediate North Atlantic general circulation. Part II: An Eulerian statistical view. *J. Phys. Oceanogr.,* **32,** 2034–2053, doi:10.1175/1520-0485(2002)032<2034:SFRMIN>2.0.CO;2.

Park, Y.-G., and K. Bryan, 2000: Comparisons of thermally driven circulations from a depth-coordinate model and an isopycnal-layer model. Part I: Scaling-law sensitivity to vertical diffusivity. *J. Phys. Oceanogr.,* **30,** 590–605, doi:10.1175/1520-0485(2000)030<0590:COTDCF>2.0.CO;2.

Phillips, N. A., 1951: A simple three-dimensional model for the study of large-scale extratropical flow patterns. *J. Meteor.,* **8,** 381–394, doi:10.1175/1520-0469(1951)008<0381:ASTDMF>2.0.CO;2.

Polzin, K., J. M. Toole, J. R. Ledwell, and R. W. Schmitt, 1997: Spatial variability of turbulent mixing in the abyssal ocean. *Science,* **276,** 93–96, doi:10.1126/science.276.5309.93.

Roberts, M. J., and Coauthors, 2004: Impact of an eddy-permitting ocean resolution on control and climate change simulations with a global coupled GCM. *J. Climate,* **17,** 3–20, doi:10.1175/1520-0442(2004)017<0003:IOAEOR>2.0.CO;2.

Sévellec, F., and A. Fedorov, 2013: The leading, interdecadal eigenmode of the Atlantic meridional overturning circulation in a realistic ocean model. *J. Climate,* **26,** 2160–2183, doi:10.1175/JCLI-D-11-00023.1.

——, T. Huck, M. Ben Jelloul, and J. Vialard, 2009: Nonnormal multidecadal response of the thermohaline circulation induced by optimal surface salinity perturbations. *J. Phys. Oceanogr.,* **39,** 852–872, doi:10.1175/2008JPO3998.1.

Shchepetkin, A., and J. C. McWilliams, 2005: The Regional Oceanic Modeling System: A split-explicit, free-surface, topography-following-coordinate ocean model. *Ocean Modell.,* **9,** 347–404, doi:10.1016/j.ocemod.2004.08.002.

Spall, M. A., 2008: Low-frequency interaction between horizontal and overturning gyres in the ocean. *Geophys. Res. Lett.,* **35,** L18614, doi:10.1029/2008GL035206.

Stammer, D., 1997: Global characteristics of ocean variability estimated from regional TOPEX/POSEIDON altimeter measurements. *J. Phys. Oceanogr.,* **27,** 1743–1769, doi:10.1175/1520-0485(1997)027<1743:GCOOVE>2.0.CO;2.

te Raa, L. A., and H. A. Dijkstra, 2002: Instability of the thermohaline ocean circulation on interdecadal timescales. *J. Phys. Oceanogr.,* **32,** 138–160, doi:10.1175/1520-0485(2002)032<0138:IOTTOC>2.0.CO;2.

Timmermann, A., M. Latif, R. Voss, and A. Grötzner, 1998: Northern Hemispheric interdecadal variability: A coupled air–sea mode. *J. Climate,* **11,** 1906–1931, doi:10.1175/1520-0442-11.8.1906.

Tulloch, R., and J. Marshall, 2012: Exploring mechanisms of variability and predictability of Atlantic meridional overturning circulation in two coupled climate models. *J. Climate,* **25,** 4067–4080, doi:10.1175/JCLI-D-11-00460.1.

Waterhouse, A. F., and Coauthors, 2014: Global patterns of diapycnal mixing from measurements of the turbulent dissipation rate. *J. Phys. Oceanogr.,* **44,** 1854–1872, doi:10.1175/JPO-D-13-0104.1.

Weaver, A. J., and S. Valcke, 1998: On the variability of the thermohaline circulation in the GFDL coupled model. *J. Climate,* **11,** 759–767, doi:10.1175/1520-0442(1998)011<0759:OTVOTT>2.0.CO;2.

Welander, P., 1986: Thermohaline effects in the ocean circulation and related simple models. *Large-Scale Transport Processes in Oceans and Atmosphere,* D. L. T. Anderson and J. Willebrand, Eds., Springer, 163–200.

Winton, M., 1997: The damping effect of bottom topography on internal decadal-scale oscillations of the thermohaline circulation. *J. Phys. Oceanogr.,* **27,** 203–208, doi:10.1175/1520-0485(1997)027<0203:TDEOBT>2.0.CO;2.

Zhang, S., C. A. Lin, and R. J. Greatbatch, 1992: A thermocline model for ocean-climate studies. *J. Mar. Res.,* **50,** 99–124, doi:10.1357/002224092784797755.